INTERNATIONAL JOURNAL FOR NUMERICAL METHODS IN FLUIDS
Int. J. Numer. Meth. Fluids 2006; **52**:639–658
Published online 17 February 2006 in Wiley InterScience (www.interscience.wiley.com). DOI: 10.1002/fld.1192

A numerical method for simulation of attached cavitation flows

Lijun Liu[1,‡], Jun Li[2,*,†] and Zhenping Feng[2,§]

[1]*Research Institute for Applied Mechanics, Kyushu University, Fukuoka 816-8580, Japan*
[2]*Institute of Turbomachinery, Xi'an Jiaotong University, Xi'an 710049, People's Republic of China*

SUMMARY

A new numerical algorithm for attached cavitation flows is developed. A cavitation model is implemented in a viscous Navier–Stokes solver. The liquid–vapour interface is assumed as a free surface boundary of the computation domain. Its shape is determined with an iterative procedure to match the cavity surface to a constant pressure boundary. The pressure distribution, as well as its gradient along the wall, is taken into account in updating the cavity shape iteratively. A series of computations are performed for the cavitating flows across three kinds of headform/cylinder bodies: conic, ogival and hemispheric heads. A range of cavitation numbers is investigated for each headform/cylinder body. The obtained results are reasonable and the iterative procedure of cavity shape updating is quite stable. The superiority of the developed cavitation model and algorithm is demonstrated. Copyright © 2006 John Wiley & Sons, Ltd.

KEY WORDS: cavitation; liquid/vapour interface tracking method; numerical simulation

1. INTRODUCTION

Cavitation is a widely existing hydrodynamic phenomenon that has received much attention over the past decades. However, it remains a persistent challenge to both researchers and designers because of its extreme complexity and daunting difficulties in experimental studies as well as numerical simulation. Cavitation physics plays an important role in the design and operation of many liquid handling turbomachines and devices. When updating existing

*Correspondence to: Jun Li, Institute of Turbomachinery, School of Energy & Power Engineering, Xi'an Jiaotong University, Xi'an 710049, People's Republic of China.
†E-mail: junli@mail.xjtu.edu.cn
‡E-mail: lxl@riam.kyushu-u.ac.jp
§E-mail: zpfeng@mail.xjtu.edu.cn

Contract/grant sponsor: Specialized Research Fund for the Doctoral Program of Higher Education (SRFDP); contract/grant number: 20040698049
Contract/grant sponsor: Natural Science Foundations of Xi'an Jiaotong University

Received 16 June 2005
Revised 27 December 2005
Accepted 31 December 2005

hydraulic installations or designing new geometries, the cavitation guarantees are often the main limiting features. A precise prediction of this phenomenon and evaluation of its deteriorative effect on the performance of machine by numerical simulation is therefore obviously essential. Accordingly, substantial efforts in this aspect [1–8] have been undertaken recently towards understanding the physics of, designing away from, and accommodating the effects of cavitation.

Among the several types of cavitation, attached cavitation (or sheet cavitation) is widely encountered in hydraulic engineering and in a variety of different situations, such as underwater vehicles, high-speed pumps and high-pressure injectors. These flows are characterized with a vapour forebody attached to the surface of an object. At the rear part of an attached cavitation, there is an unsteady, two-phase and turbulent wake region where the cavitation bubble begins to collapse under the influence of increasing external pressure. A bulk of researches has been carried out to date to deal with cavitating flows of this nature [7–15].

Recently, with the advent of inexpensive powerful computers and urgent request for understanding the physics of cavitation, more general computational fluid dynamics (CFD) approaches have been developed and they are seeing more and more use in predicting flow fields of this nature in different liquid handling machines and situations. Deshpande *et al.* [14] developed an Euler analysis method and then extended it by solving the Reynolds-averaged Navier–Stokes (RANS) equations to predict the geometrical characteristics of cavitation bubble. Chen and Heister [15] developed some effective numerical techniques for attached cavitation. In addition, in the past decade, a bulk of works [4, 8, 12, 13] has been performed for cavitating flows by RANS methodologies. The most attractive features of RANS methodologies are that many realistic physics of cavitation can be readily incorporated and modelled, and, they are feasible for application in very complicated configurations. The wall detachment point and bubble length are naturally determined from the computation, unlike the potential model in which they are usually given as *a priori* knowledge.

The adaptations of RANS methodologies for modelling attached cavitating flows can be grouped into two distinctly different approaches. One approach, which is often referred to as interface capturing method, treats the flow as a compressible continuum fluid with variable properties and a pseudo-density that widely varies between liquid and vapour extremes. The entire flow field is discretized and described by a set of compressible Navier–Stokes equations. The most attractive features of this approach are that no *ad hoc* wake closure model is required and it can treat travelling cavitations as well as attached cavitations. In addition, the computation is performed on a set of fixed mesh. Much progress of this approach has been achieved recently [4, 6]. Some adaptations of the interface capturing approach have been incorporated in some commercial CFD software packages [16].

Another distinct class of numerical method, hereafter referred to as interface tracking approach, seeks a solution in the liquid domain along with a description of the boundary of the cavitating area. The liquid/vapour bubble interface is treated as part of the boundary of the computation domain. It is determined with an assumption that the cavitating region is at a constant pressure equal to the local vapour pressure. The flow field is solved with a single-phase flow solver. Because of the nonlinear relationship between the vapour cavity shape and the external flow field of liquid, the solution of interface shape is obtained with an iteration procedure. The interface is updated iteratively until a unique convergent shape is achieved with constant pressure along it. Numerically, however, the interface tracking approach has to employ a wake closure model to approximate the two-phase behaviour in the

wake region at the rear of the cavitation region, since it is impossible to impose a constant pressure condition on the entire cavity surface while the recovery of pressure occurs at the aft end of the cavitation. Despite that it is difficult to introduce physics into the wake closure model and there is no general way to define it, most authors [17, 18] agree that the choice of the wake closure model has little influence on the forebody of cavity and their researches have proved this assertion.

The most salient feature of the interface tracking approach is that it has bypassed all those numerical difficulties of the interface capturing approach and physical modelling difficulties of the two-phase flow models. Meanwhile it retains the capability to capture most features of the viscous attached cavitating flows. Numerous excellent works [14, 17, 18] have been carried out to refine this cavitation model towards studying the physics of cavitation. Besides the computational efficiency of the interface tracking approach, it can predict the overall behaviour of cavitating flows fairly well [17]. In particular, since only the incompressible single-phase flow solver, which is relatively simple and well developed, is applied, the numerical treatments of interface tracking schemes and computation algorithms are much more mature than that of the two-phase flow models and interface capturing techniques. In addition, since the implementation of interface tracking schemes is independent of the flow solver, it is easy to be incorporated with any existing flow solvers or commercial software packages.

In this paper, we implemented the interface tracking approach with a turbulent incompressible RANS flow solver. A new cavity shape updating formulation was developed. The cavitation model and some improved numerical treatments were presented after a brief description of the flow solver. Then, a series of computation results was shown for the cavitating flows past a variety of axisymmetric headform/cylinder bodies. The accuracy of the algorithm and cavitation model was well validated with comparisons between the computation results and available experimental data.

2. RANS FLOW SOLVER

The mass conservation equation and momentum equations can be written as follows in Cartesian coordinates for steady, incompressible viscous flows:

$$\frac{\partial(\rho u_i)}{\partial x_i} = 0 \tag{1}$$

$$\frac{\partial(\rho u_j u_i)}{\partial x_j} = -\frac{\partial p}{\partial x_i} + \frac{\partial \tau_{ij}}{\partial x_j} \tag{2}$$

where $\tau_{ij} = \mu_{\text{eff}}((\partial u_i/\partial x_j) + (\partial u_j/\partial x_i)) - \frac{2}{3}\delta_{ij}\mu_{\text{eff}}(\partial u_l/\partial x_l)$, $\mu_{\text{eff}} = \mu + \mu_t$, μ and μ_t are molecular and turbulent viscosity, respectively.

As a cavitating flow is concerned, the most turbulence-dominated area is in the wake region of a cavitation. Actually, the vapour bubble suddenly collapses in this region and strongly interacts with the solid wall. The flow is two-phase, turbulence-dominated and strongly time-dependent. The mechanisms of this kind of two-phase flows are extremely complex in this region and no available turbulence model is capable of treating this kind of turbulent flow properly [18]. In our model, this area is modelled with a wake closure model since the condition of constant pressure equal to the vapour pressure is impossible to meet along the

entire cavity surface from the view point of simulation. In addition, the Reynolds number of flows of the calculation examples in this work is very small. The turbulence effect is negligible. So we just used an algebraic turbulence model to approximate the effect of turbulence on the flow. The Baldwin–Lomax turbulence model [19] is employed to approximately evaluate the turbulence viscosity due to its simplicity and computational efficiency. The well-known wall-function method is used to model the flow close to solid walls. The algebraic Baldwin–Lomax turbulence model coded in the program is given by

$$\mu_t = 0.16\rho y^2[1 - \exp(-y^+/A^+)]^2|\Omega|, \quad 0 \leqslant y \leqslant y' \tag{3a}$$

$$\mu_t = 0.02688\rho F_w \left[1 + 5.5\left(\frac{0.3y}{y_{max}}\right)^6\right]^{-1}, \quad y \geqslant y' \tag{3b}$$

where y denotes the normal distance away from the wall. Formulation (3a) denotes the inner layer of the wall region and formulation (3b) denotes the outer layer. The parameter y' represents the smallest value of y at which the values of μ_t in the inner and outer layer are equal to each other. The parameter y^+ is defined as

$$y^+ = \frac{\sqrt{\rho_w \tau_w}}{\mu_w} y, \quad A^+ = 26$$

where τ_w and μ_w are the shear stress and molecular viscosity at the wall. Parameter Ω is the strength of flow vortex, and

$$F_w = \left\{\frac{0.25 y_{max}(U_{max} - U_{min})^2}{F_{max}}\right\} \quad \text{or} \quad F_w = y_{max}F_{max}$$

The smaller one of the two values of F_w is taken. Here, F_{max} is the maximum value of the function

$$F(y) = y|\Omega|[1 - \exp(-y^+/A^+)]$$

and y_{max} is the value of y at that point.

Using the technique of non-staggered grid, a pressure-based algorithm based on the so-called SIMPLEC method for general curvilinear coordinates is adopted to couple the momentum equations and the continuity equation in the flow computations [20]. The covariant velocity projections rather than the Cartesian velocity components are selected as the dependent variables, resulting in the cross-pressure gradient terms in the momentum equations disappear. The pressure correction, rather than the pressure itself, is derived and solved in this method. A momentum interpolation scheme, which was newly developed to suppress the nonphysical pressure oscillation, is used for getting the flow flux through the surfaces of the control volume. The discretization of the governing equations is performed using the finite volume approach. The convective and the orthogonal diffusion terms in the momentum equations are treated by using the two-order upwind differencing scheme. The non-orthogonal diffusion terms are evaluated by using the central differencing scheme and lumped into the source term of the discretization equations. The resulting discretization equations are solved iteratively by

the successive line over-relaxation (SLOR) method, with ADI and block additive correction technique to speed up the convergence speed.

Neumann boundary condition is imposed for pressure correction on all boundaries. The inlet pressure level is prescribed. A uniform velocity field is defined at the inlet boundary and Neumann condition is specified at the outlet boundary. The non-slip condition is applied on all wall surfaces. The cavity surface is treated as a free streamline. So the free surface boundary condition and impermeability condition are applied on the cavity surface. That is $\partial V_t/\partial n = 0$ and $V_n = 0$, where n is the normal direction and t is the tangential direction to the local surface of cavity.

3. CAVITATION MODEL AND ALGORITHMS

The attached cavitation is modelled as a large cavity bubble on the wall with an interface to the bulk flow. Basically, there are three assumptions in this cavitation model,

(1) The cavity surface (or the interface) is a free surface.
(2) The pressure inside the cavity equals the local vapour pressure of fluid. In other word, if the cavity surface is treated as a boundary of the computation domain, the pressure on this part of boundary is equal to the vapour pressure.
(3) The rear part of the cavitation bubble is approximated with a wake model, where the pressure is no longer equal to the vapour pressure.

Presented in Figure 1 is a schematic description of a cavitation bubble on a headform/cylinder body, where A is the inception point, B the point linking the forebody and afterbody (wake region) of the cavity and C the end point of cavitation. Obviously, there are three highlights needed to pay attention to construct the cavity profile: the location of inception point A, the profile of the forebody $\overline{AB}$ and the profile of the afterbody $\overline{BC}$.

In our computations, the inception point is located by searching for the point on the currently non-cavitation wall, where the pressure is minimal and drops below the local vapour pressure. During the iteration of the cavity shape updating, the located inception point tends to move upstream on a smooth wall with the establishing of the cavity shape. If the cavitation occurs downstream to a sharp corner of a wall, the inception point often occurs at the sharp corner

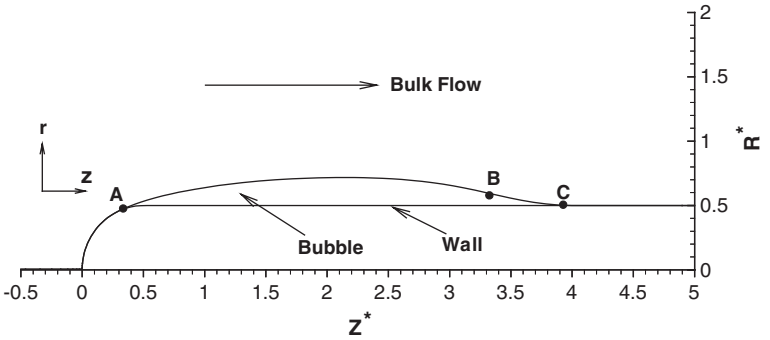

Figure 1. A schematic of the cavitation model.

and always remains at the corner point. The computations showed this locating method for the inception point is efficient and effective.

Regarding the two-phase turbulent wake region, since we are still not aware of the flow structure and mechanisms in it, it is modelled by an afterbody defined by a cubic polynomial function for the sake of simplicity [14, 17, 18]. The afterbody begins at the point on the cavity surface where the local height is, for example, half of the maximal height of the cavity. It smoothly links the forebody of the cavity and the local wall surface. The first and the second derivatives of the cavity profile at the linking point B are enforced to be continuous. The length of the closure domain, as well as the attached point of the cavity, is automatically determined by the wake closure model. However, at the early stage of iteration, since the cavity shape is far from well established, the length of the closure domain calculated from the wake closure model may be too long or too short. This will result in both the inner loop iteration of the flow field calculation and the outer loop iteration of the cavity shape updating time-consuming and instable. In order to avoid this numerical problem, the length of the wake region is specified associating with the maximal height of the cavity and only the first derivation of the cavity profile at the linking point B is enforced to be continuous. The computations showed that this technique can speed up the iterations of both the inner loop and outer loop.

Because of the strong interaction between the cavity shape and the bulk flow around it, the forebody of the cavity is established iteratively by using a cavity shape updating scheme. The solution of the cavity shape and flow field is achieved until the pressure on the cavity surface converges to a constant value equal to the vapour pressure of fluid. The free surface boundary condition is applied on the cavity surface.

Numerically, this algorithm is to enforce the pressure on the forebody of the cavity surface approach to a constant value equal to the local vapour pressure by establishing a proper cavity shape iteratively. In other words, the following conditions must be satisfied when the convergent solution of the cavity shape is obtained.

(1) The pressure on the forebody of the cavity surface is uniformly distributed, approaching to a constant value.
(2) This value is equal to the local vapour pressure of fluid.

Obviously, the first condition specifies the uniformity of the pressure on the cavity surface and the second condition specifies the level of the pressure. Thus, it is natural to consider using the feedback information of both pressure and pressure gradient distribution on the cavity surface from the flow computation when updating the cavity shape.

In order to verify the influence of cavity length and height on the pressure distribution, we carried out the flow field in a flow channel with a bump on its bottom wall as shown in Figure 2. The bump on the wall of the flow channel corresponds to the cavity in a cavitating flow. We changed the height and length of the bump to compare their influence on the pressure distribution on the bottom wall. The results are shown in Figure 2 from which we can know that both the height and length of the bump have obvious influence on the pressure distribution on the wall. In our model, the height and length of the cavity are obtained with a coupled iterative procedure. Only the height of cavity has been established, then the length of cavity can be determined because of the influence of cavity shape on the pressure distribution on the body.

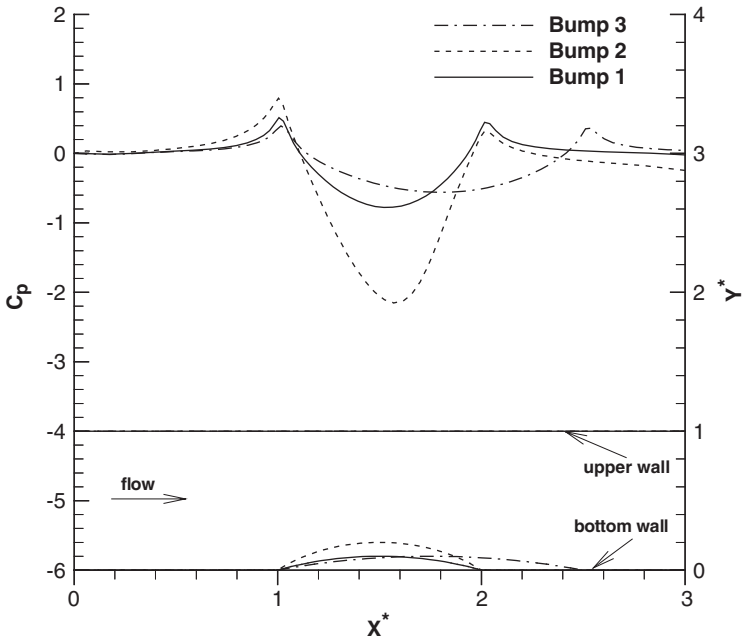

Figure 2. Influence of a bump shape on the pressure distribution on the wall of a channel.

In order to derive the formulation in a more general way, we write the relationship between the cavity shape and the pressure distribution along it as follows, without loss of generality for a given flow condition and geometrical configuration:

$$f\left(r, \frac{\partial r}{\partial s}, \frac{\partial^2 r}{\partial s^2}, \frac{\partial^3 r}{\partial s^3}, \ldots, p, \frac{\partial p}{\partial s}, \frac{\partial^2 p}{\partial s^2}, \frac{\partial^3 p}{\partial s^3}, \ldots\right) = 0 \tag{4}$$

where $r(s)$ and $p(s)$ are the local thickness of cavity and the local pressure around it, s is the distance coordination along the wall in the bulk flow direction.

Considering n the superscript corresponding to the calculated value of the present iteration of cavity shape updating, we have,

$$f\left(r^{(n)}, \frac{\partial r^{(n)}}{\partial s}, \frac{\partial^2 r^{(n)}}{\partial s^2}, \frac{\partial^3 r^{(n)}}{\partial s^3}, \ldots, p^{(n)}, \frac{\partial p^{(n)}}{\partial s}, \frac{\partial^2 p^{(n)}}{\partial s^2}, \frac{\partial^3 p^{(n)}}{\partial s^3}, \ldots\right) = 0 \tag{5}$$

Since the pressure distribution $p^{(n)}(s)$ does not meet the pressure boundary condition along the cavity surface and deviates from the local vapour pressure p_V, we need to modify the cavity shape as

$$r^{(n+1)} = r^{(n)} + \Delta r^{(n)} \tag{6}$$

so that

$$p^{(n+1)} = p_V \tag{7}$$

Meanwhile, when Δr is a value small enough, we can operate the function expressed in (4) like a linear function without loss of generality. Substituting the relationships (6) and (7) into (4), and then subtract (5) from it, we obtain

$$f\left(\Delta r^{(n)}, \frac{\partial \Delta r^{(n)}}{\partial s}, \frac{\partial^2 \Delta r^{(n)}}{\partial s^2}, \frac{\partial^3 \Delta r^{(n)}}{\partial s^3}, \ldots, p_V - p^{(n)}, -\frac{\partial p^{(n)}}{\partial s}, -\frac{\partial^2 p^{(n)}}{\partial s^2}, -\frac{\partial^3 p^{(n)}}{\partial s^3}, \ldots\right) = 0 \tag{8}$$

Drop the high order terms of small value in the above expression and rewrite it as

$$\begin{aligned} &\alpha_0 \Delta r^{(n)} + \alpha_1 \frac{\partial \Delta r^{(n)}}{\partial s} + \alpha_2 \frac{\partial^2 \Delta r^{(n)}}{\partial s^2} + \alpha_3 \frac{\partial^3 \Delta r^{(n)}}{\partial s^3} + \cdots \\ &\quad = \beta_0 (p_V - p^{(n)}) + \beta_1 \frac{\partial p^{(n)}}{\partial s} + \beta_2 \frac{\partial^2 p^{(n)}}{\partial s^2} + \beta_3 \frac{\partial^3 p^{(n)}}{\partial s^3} + \cdots \end{aligned} \tag{9}$$

where $\alpha_0, \alpha_1, \alpha_2, \ldots, \beta_0, \beta_1, \beta_2, \ldots$ are coefficients of each term in the expression. These coefficients are functions of the cavity shape and pressure distribution at each iteration step. They can be calculated out at each iteration step from the current solution of the flow field and the cavity shape by solving the following equation at each grid point on the cavity surface:

$$\begin{aligned} &\alpha_0 r^{(n)} + \alpha_1 \frac{\partial r^{(n)}}{\partial s} + \alpha_2 \frac{\partial^2 r^{(n)}}{\partial s^2} + \alpha_3 \frac{\partial^3 r^{(n)}}{\partial s^3} + \cdots \\ &\quad = \beta_0 p^{(n)} - \beta_1 \frac{\partial p^{(n)}}{\partial s} - \beta_2 \frac{\partial^2 p^{(n)}}{\partial s^2} - \beta_3 \frac{\partial^3 p^{(n)}}{\partial s^3} - \cdots \end{aligned} \tag{10}$$

Theoretically, after obtaining these coefficients by solving Equation (10) at each grid point on the cavity surface with the current cavity shape and pressure distribution, we can get the newly updated cavity shape from Equation (9). Formulations (9) and (10) therefore constitute the newly proposed cavity shape updating scheme, from which the adjustment value of the cavity shape can be calculated with the current calculated flow field.

As mentioned above, the adjustment value of Δr must be small enough in order to ensure the above scheme valid. Therefore, it is necessary to use the following formula to modify the cavity shape iteratively,

$$r^{(n+1)} = r^{(n)} + \tilde{\lambda} \Delta r^{(n)} \tag{11}$$

where $\tilde{\lambda}$ is a relaxation factor less than one.

Obviously, it is tedious to solve Equations (9) and (10) if too many terms are included. Furthermore, the mesh resolution has to be very fine if high-order derivatives are included in the equations, resulting in the computation load increase dramatically. So it is necessary to approximate the scheme in a simple but effective way.

Approximate formula (9) and (10) by dropping all those terms of high-order derivative and rewrite them as

$$\alpha_0 \Delta r^{(n)} + \alpha_1 \frac{\partial \Delta r^{(n)}}{\partial s} \cong \beta_0 (p_V - p^{(n)}) + \beta_1 \frac{\partial p^{(n)}}{\partial s} \tag{12}$$

$$\alpha_0 r^{(n)} + \alpha_1 \frac{\partial r^{(n)}}{\partial s} \cong \beta_0 p^{(n)} - \beta_1 \frac{\partial p^{(n)}}{\partial s} \tag{13}$$

The coefficients are calculated from the current flow computation and the cavity shape by Equation (13). In a simpler way, they can also be simply specified as empirical constants for a given flow condition and configuration. If one gives $\alpha_0 = 1$, $\alpha_1 = 0$ and $\beta_1 = 0$, Equation (12) becomes

$$\Delta r^{(n)} = \beta_0 (p_V - p^{(n)}) \tag{14}$$

Formula (14) corresponds to the formula proposed by Hirschi *et al.* [17]. If one gives $\alpha_0 = 0$, $\alpha_1 = 1$ and $\beta_1 = 0$, Equation (12) becomes

$$\Delta \alpha^{(n)} \cong \frac{\partial \Delta r^{(n)}}{\partial s} = \beta_0 (p_V - p^{(n)}) \tag{15}$$

Formula (15) corresponds to the formula proposed by Chen and Heister [18]. That is to say, the existing schemes are some special simplified forms of formula (12) and they did not take into account the pressure gradient.

For simplicity and ease to be coded, let $\alpha_0 = 0$ and $\alpha_1 = 1$ so that Equation (12) becomes

$$\Delta \alpha \cong \frac{\partial \Delta r^{(n)}}{\partial s} = \beta_0 (p_V - p^{(n)}) + \beta_1 \frac{\partial p^{(n)}}{\partial s} \tag{16}$$

Integrating Equation (16) along the cavity surface from the inception point gives,

$$\Delta r^{(n)} = \int_{s_b}^{s} \left[\beta_0 (p_V - p^{(n)}) + \beta_1 \frac{\partial p^{(n)}}{\partial s} \right] \mathrm{d}s \tag{17}$$

where s_b is the location of the inception point. As can be seen, the pressure difference, as well as the pressure gradient along the cavity surface, is taken into account to determine the adjustment value of cavity shape. The scheme of formula (17) is thus superior to the existing schemes in which only the pressure difference is considered.

By analysing the two terms on the right hand of Equation (16), it is easy to determine the signs of coefficients β_0 and β_1. The first term is the pressure difference between the inside and outside of the cavitation bubble. When $p_V \geqslant p^{(n)}$ and neglecting the surface tension, the bubble tends to grow, and vice versa. Thus, the sign of β_0 is positive. The second term is the pressure gradient along the cavity surface. According to the relationship between the pressure gradient and the gradient of cavity thickness distribution, the sign of β_1 is also positive.

In order to stabilize the numerical iteration and make the formula to be more general for different flow conditions and geometrical configurations, formula (17) is further modified as

$$\Delta r^{(n)} = \frac{\pi}{180} \int_{s_b}^{s} \left(\beta_0' \operatorname{sign}(p_V - p^{(n)}) \sqrt{\frac{|p^{(n)} - p_V|}{\|p^{(0)} - p_V\|}} + \beta_1' \operatorname{sign}\left(\frac{\partial p^{(n)}}{\partial s} \right) \sqrt{\frac{|\partial p^{(n)}/\partial s|}{\|\partial p^{(0)}/\partial s\|}} \right) \mathrm{d}s \tag{18}$$

where $\|p^{(0)} - p_V\| = \sqrt{\int_{s_b}^{s_e} (p^{(0)} - p_V)^2 \, ds/(s_e - s_b)}$ and $\|\partial p^{(0)}/\partial s\|$ is defined in the same way, and s_e is the end point of cavitation. All computations of this work were carried out using the formula expressed in (18). The iteration of cavity shape adapting is stable. The factors β_0', β_1' are specified in a range from 0.1 to 1.0, depending on the flow conditions and configurations.

4. NUMERICAL ALGORITHM FOR ATTACHED CAVITATION

The treatments of cavity prediction are done independent from the flow computation in the presented method. A subroutine is coded to transfer information between the flow solver and the block of cavity shape updating and grid adjustment. Because of the strong nonlinear interaction between the cavity shape and the bulk flow around it, an iterative process is applied between the flow computation and the cavity shape updating. Basing on the pressure distribution along the cavity surface obtained from the flow computation, a cavity shape updating scheme is used to modify the cavity shape in order to match the pressure on the cavity surface to a constant value equal to the local vapour pressure of fluid. After each cavity shape modification, the mesh of the flow domain is modified to fit the new cavity profile. A new flow computation is then performed using the previous solution interpolated on the new mesh as the initial flow field. The inception point of cavitation and the cavity length are automatically determined in this iterative procedure.

The solution procedure can be outlined in four steps as follows:

(1) A cavitation free flow computation is performed. According to the information given by the flow computation, the cavitation area as well as its inception point is located. The point on the wall where the pressure is locally minimal and drops below the vapour pressure is treated as the inception point. All the points downstream of the inception point are activated to be in the cavitation area if the pressure is below the vapour pressure. The thickness of the cavity is initially assumed to be zero in the cavitation area. The initial mesh is saved as the background mesh for the later interpolation operations.

(2) Flow computation is repeated, enforcing the free surface boundary condition on the cavity surface.

(3) Check if the pressure distribution on the cavity surface has converged to the vapour pressure in a prescribed permission error. If it has converged, that means the proper cavity shape has been established. Then we terminate the computation and output the final results. Otherwise, according to the feedback information from the flow computation, the cavity shape is modified using the proposed cavity shape updating scheme. Meanwhile, the location of the inception point is again checked and relocated if necessary. The wake model is used to redefine the afterbody according to the new cavity shape. The current solution of the flow field is stored on the background mesh. For the case of multiple cavitation regions, it is necessary to check if new cavitation region has appeared on the wall surface. In other words, check if there is any other point on the wall that is not in the existing cavitation regions and has a locally minimal pressure lower than the vapour pressure.

(4) The mesh is re-constructed to adapt to the new cavity surface. The previous solution of the flow field stored on the background mesh is then interpolated on the new mesh as the initial field for the flow computation of the next cycle.

The process from steps (2) to (4) is repeated until the pressure distribution on the cavity surface approaches to a constant value equal to the vapour pressure in a prescribed permission error. The iteration process is terminated when the solution of the flow field has converged and the following condition gets satisfied:

$$D_p/D_{p_0} = \frac{\| p^{(n)}(s) - p_V \|}{\| p^{(0)}(s) - p_V |} \leqslant \delta \tag{19}$$

where $p(s)$ is the pressure on the forebody of the cavity, p_V is the vapour pressure, δ presents the prescribed permission error. $\| p(s) - p_V \|$ is the second modulus of pressure difference over the forebody of the cavity surface. δ is a value between 5×10^{-3} and 3×10^{-2}.

In this work, an algebraic method is chosen for mesh generation due to its computational efficiency. Exponential stretching is used in high-gradient regions. A typical mesh is shown for an axisymmetric hemispheric headform/cylinder body in Figure 3, in which the grid is clustered near the centreline/wall surface and in the vicinity of the hemispheric headform. The initial mesh (shown in Figure 3) generated for the cavitation free flow computation is save as the background mesh. All the operations of mesh adaptation and data transferring between the previous and the next initial solution of the flow computation are performed referring to the background mesh in the iteration procedure. After each time the cavity shape has updated, the new profile of the cavity shape is recorded on the background mesh frame and the mesh is adapted to the new flow domain referring to the background mesh. Figure 4 gives a typical local mesh distribution re-grided to adapt to the cavity shape establishment on the wall of a hemispherical headform/cylinder body. The grid is clustered close to the body wall and headform where gradient is usually large. Good grid quality is ensured close to the head form with respect to the grid uniformity and skewness.

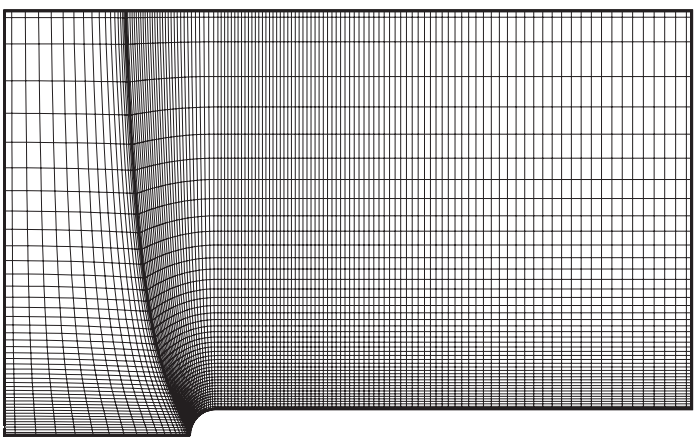

Figure 3. Mesh for cavitation free flow computation.

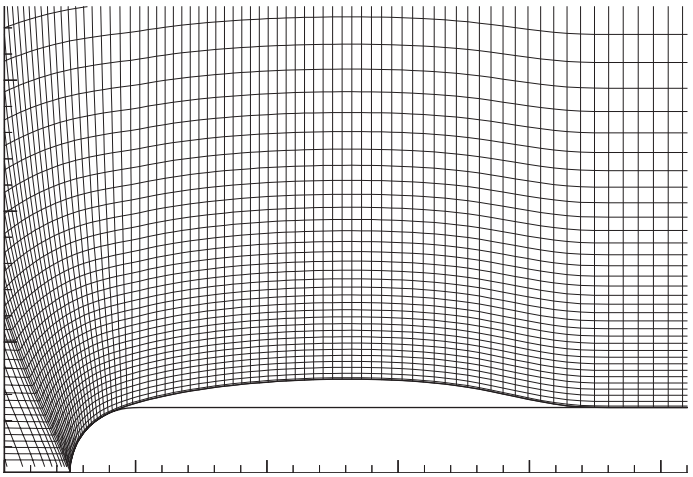

Figure 4. Local mesh distribution with cavitation.

5. VALIDATION OF THE DEVELOPED NUMERICAL METHOD

5.1. Grid numbers test

Before each computation, it is a routine to perform a mesh dependency test in order to pursue a solution independent of the mesh size employed. The computational grid is shown in Figure 5 with a grid resolution of 46×131. Figure 6 shows the mesh dependency test of the cavitation prediction for a hemispheric headform/cylinder body. Given in Figure 6 are the pressure coefficient C_p and cavity thickness distribution obtained with three sets of mesh: 32×91, 46×131 and 62×181. The cavitation index is $K = 0.20$. Here we defined $K = (p_\infty - p_V)/(p_0 - p_\infty)$ and $C_p = (p - p_\infty)/(p_0 - p_\infty)$, where p_∞ is the far-field pressure, p_0 is the total pressure and p_V is the vapour pressure. The experimental data of Rouse and McNown [9] are also presented in the figure. It is obvious that the results obtained with a mesh size of 46×131 agree very well with those obtained with a mesh size of 62×181. However, the results obtained with a mesh size of 32×91 obviously deviate away from those of the former two ones. This means that the solution is independent of the mesh size if the mesh size is larger than 46×131 for this situation.

5.2. Relaxation factors test

One of the salient originality of this work is the developed cavity shape updating scheme, in which not only the pressure difference but also the pressure gradient obtained from the previous solution of flow field are considered in modifying the cavity shape. Hereinafter, we test the efficiency of this new scheme using different relaxation factors. The influence of the relaxation factor in the formula on the performance of this scheme is also checked. The test computations are performed for a hemispheric headform/cylinder body.

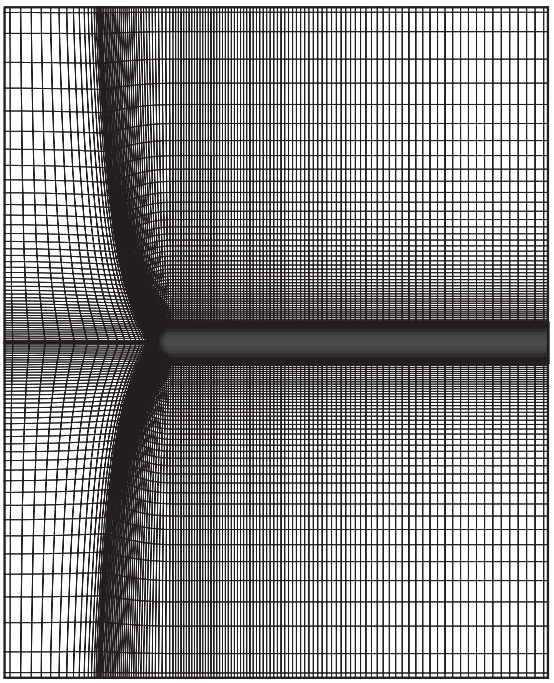

Figure 5. The computation mesh for a hemispheric headform/cylinder body with a grid resolution of 46×131.

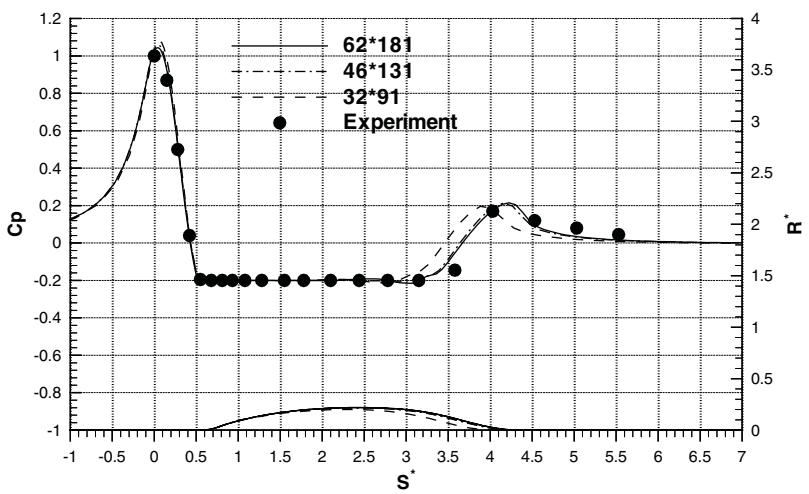

Figure 6. Comparisons of pressure distribution and cavity shape with different grid resolutions.

Assuming $\beta'_1 = \beta'_0$, formulation (18) can be rewritten as follows after making derivation calculus on its both sides while r is replaced by α,

$$\Delta\alpha^{(n)} = \frac{\pi}{180}\beta' \left[\text{sign}(p_V - p^{(n)}) \sqrt{\frac{|p^{(n)} - p_V|}{\|p^{(0)} - p_V\|}} + \text{sign}\left(\frac{\partial p^{(n)}}{\partial s}\right) \sqrt{\frac{|\partial p^{(n)}/\partial s|}{\|\partial p^{(0)}/\partial s\|}} \right] \tag{20}$$

This is the formulation of the newly developed cavity shape updating scheme used in this work. In the calculations carried out in this paper, we assumed there is no pressure difference between the two sides of cavity interface. So the forebody of the cavity surface is modelled as a boundary with constant pressure equal to the vapour pressure of fluid. When the surface tension and viscous effects are taken into account, the pressure difference between the two sides of the cavity interface is not zero and the pressure along the cavity surface is not constant any more. In this case, the parameter p_V in the cavity shape updating scheme (20) changes to a function of p_V, surface tension and viscous stress. The surface tension effect is not taken into account in the present model. The presented cavitation model and algorithm is restricted to the steady flow.

The presented cavitation updating scheme is applied for the cavitation prediction of a hemispheric headform/cylinder body for $K = 0.20$. A range of relaxation factor values is used to check their influence on the efficiency of the scheme. The iteration histories of the cavity shape updating procedure are shown in Figure 7, in which Igrid is the time number of cavity shape updating. We can see that the convergence speed tends to speed up with a larger value of relaxation factor. However, the reachable convergence precision decreases (value increases) with the increasing value of relaxation factor. For example, the convergence criteria prescribed in this work ($\log_{10} D_p/D_{p_0} = -2.0$) can be achieved with 214 iterations of cavity shape updating for $\beta' = 0.2$, while only half iteration times is needed for $\beta' = 0.5$. For $\beta' = 2.0$,

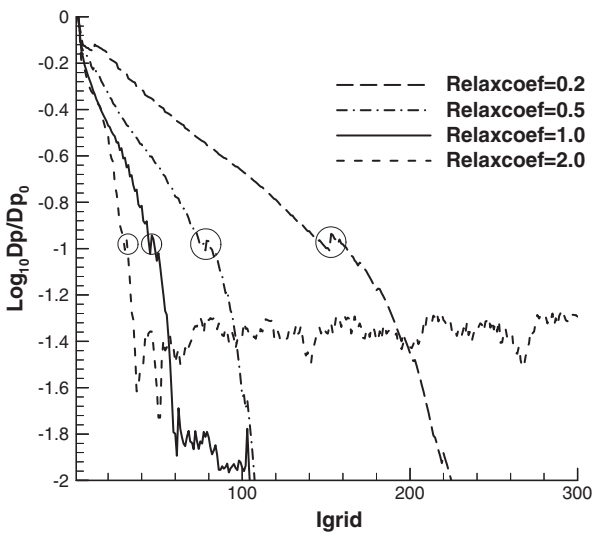

Figure 7. Comparison of iteration history with different relaxation factors.

only 33 iteration times is needed for this scheme to reach a convergence precision around $\log_{10} D_p/D_{p_0} = -1.4$, which is the limit of convergence precision with this relaxation factor. Therefore, there has a compromise between the convergence precision and computational efficiency when considering the selection of the relaxation factor. A value of $\beta' = 0.5$ is chosen to ensure the iteration converge satisfactorily. A local, small but sudden, oscillation on the curve of iteration history, as marked in the figure, is due to the transition of the defining method of the wake closure model when the iteration approaches to convergence. We can see from the figure that, the iteration seems to speed up after the transition of the defining method of the wake closure model since the profile becomes smoother. This verifies the effectiveness of the developed wake closure model.

It is worthy to be aware that the cavity shape updating scheme, as well as the choice of the empirical factors in it, plays an important role in determining the efficiency and effectiveness of the iteration algorithm. But it has no influence on the final solutions of the cavity shape and flow field only if both the flow field and the cavity shape updating procedure get satisfactorily converged.

5.3. *Headform/cylinder cavitating flows tests*

The accuracy of this cavitation model and scheme is further verified by performing cavitation predictions for a series of headform/cylinder bodies. Experimental data is reported by Rouse and McNown [9]. The experiment is conducted in a water tunnel with cylindrical test objects 0.025 m in diameter and 0.2038 m in length. The curvature radium of the ogive headform profile is two times of the radium of the after-body cylinder. For sharp edged bodies, the cavitation always occurs just downstream of the edge corner. The inception point always retains at the corner point. Here we present the results of the cavitating flows past a cone/cylinder body for $K = 0.50$, 0.40, 0.30. The apex angle of the cone is 45°. Figure 8 shows the comparison of the calculated pressure distributions along the wall surface for cavitation free flows past a cone/cylinder body with the experimental data of Rouse and McNown [9]. A comparison of the computation results is made in Figure 9 with available experimental data for $K = 0.50$, 0.40, 0.30. The comparison shows good agreement between the present computation and the measurement. A local enlargement plot of the cavity shape comparison between the computation and the experiment is given in Figure 10 for $K = 0.40$. As can be seen from the figures, the pressure distribution and cavity shape are both well duplicated with the present model as compared with the experimental results. Even the pressure recovery in the wake region is well predicted. Different cavity shapes along the cone/cylinder for three different cavitation index $K = 0.50$, 0.40, 0.30 are shown in Figure 11. The strong influence of cavitation on the pressure distribution and the flow pattern is highlighted in Figures 9 and 11.

For sharp-edged body, the inception point is always at the corner. It is more challenging to predict the inception point of cavitation for a smooth body. To test the model and treatments in such cases, we performed computations for an Ogival headform/cylinder body for $K = 0.32$, 0.24 and a hemispheric headform/cylinder body for $K = 0.40$, 0.30, 0.20. The curvature radium of the ogive headform profile is two times of the radium of the afterbody cylinder.

Figure 12 gives the pressure coefficient distribution, cavity thickness distribution for an ogive/cylinder body for $K = 0.32$, 0.24. The results of a free cavitation computation and the experimental data were also included for comparison. Figure 13 shows the cavity shape along the ogive/cylinder body with $K = 0.32$, 0.24. Figures 14 and 15 present the pressure

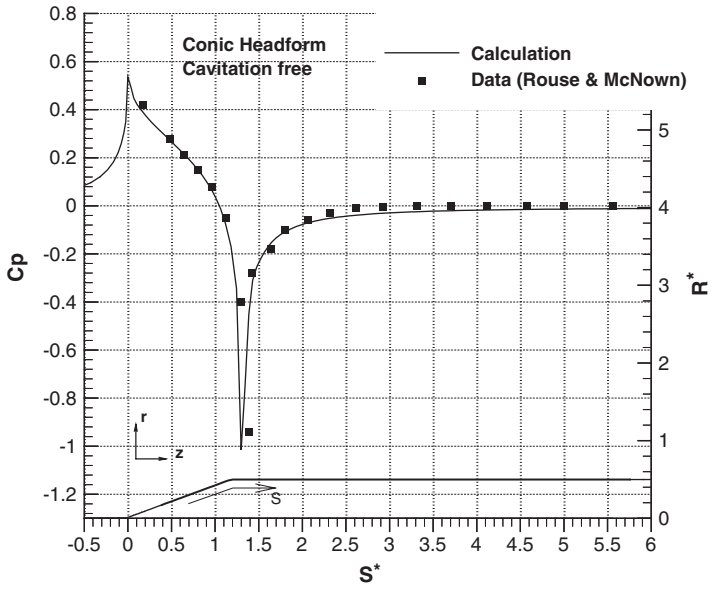

Figure 8. Pressure distribution for a conic headform/cylinder body without cavitation.

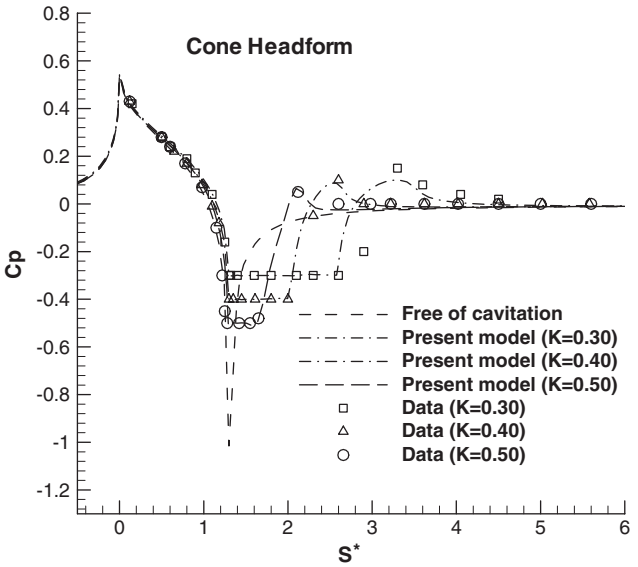

Figure 9. Pressure distribution and cavity shape for a conic headform/cylinder body.

distribution, cavity thickness distribution and cavity shape for a hemisphere/cylinder body for $K = 0.40$, 0.30, 0.20, respectively. The results of the free cavitation computation and the experimental data are included for comparison. Results in these figures indicate that the location of inception point is accurately predicted for cavitation on these smooth surfaces. These results

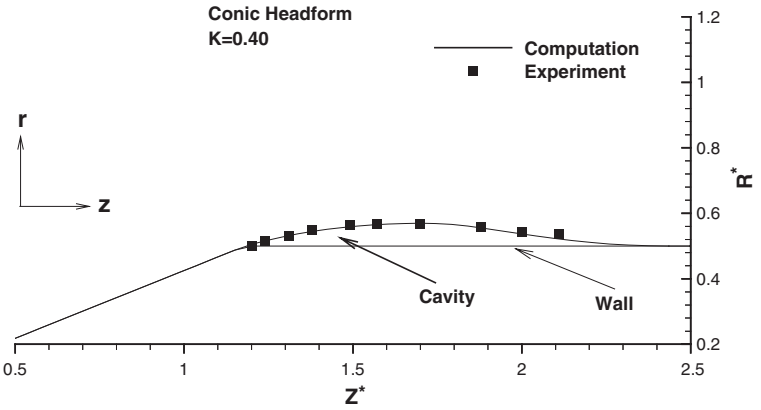

Figure 10. Comparison of the calculated cavity shape with experiment data ($K = 0.40$).

Figure 11. Cavity shapes on the wall of a conic headform/cylinder body with different cavitation indexes: (a) $K = 0.30$; (b) $K = 0.40$; and (c) $K = 0.50$.

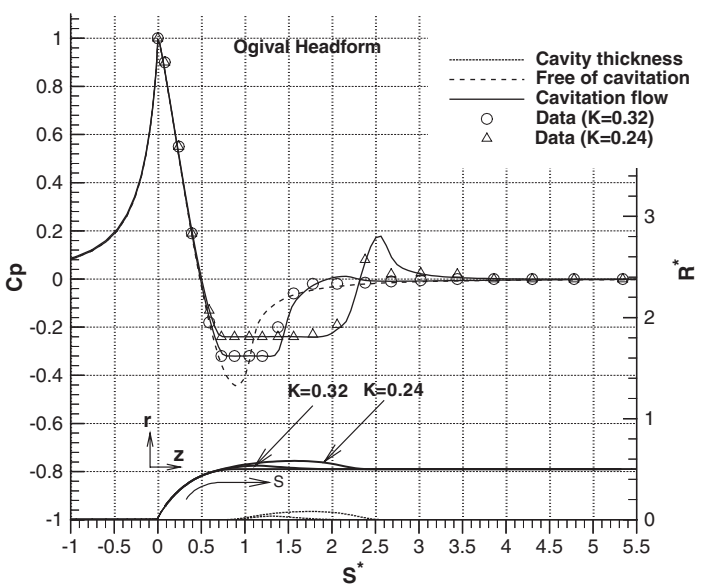

Figure 12. Pressure distribution and cavity shape for an ogival headform/cylinder body.

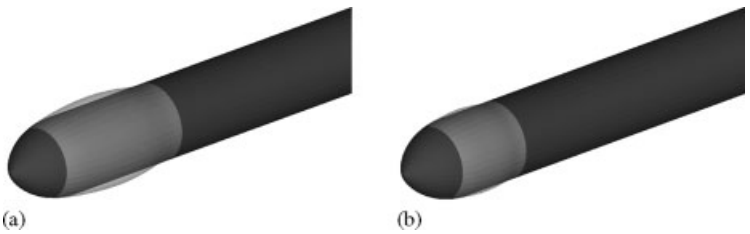

Figure 13. Cavity shape on the wall of an ogival headform/cylinder body with different cavitation indexes: (a) $K = 0.24$; and (b) $K = 0.32$.

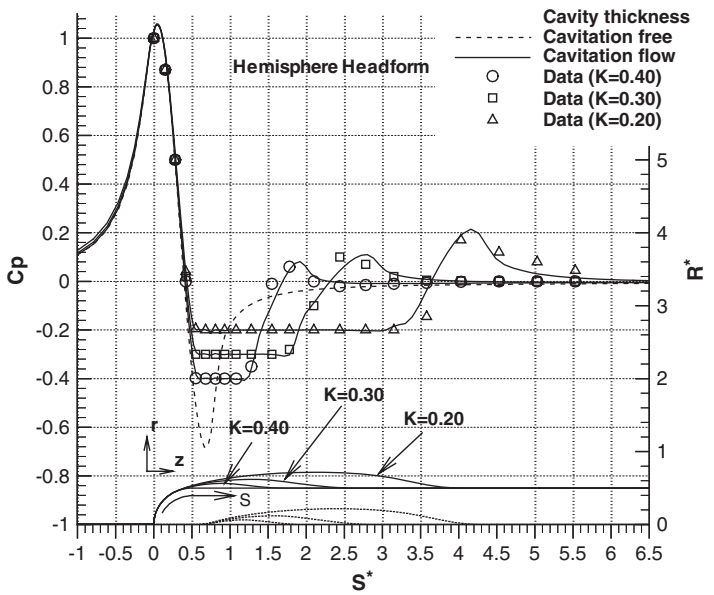

Figure 14. Pressure distribution and cavity shape for a hemispheric headform/cylinder body.

Figure 15. Cavity shapes on the wall of a hemispheric headform/cylinder body with different cavitation indexes: (a) $K = 0.20$; (b) $K = 0.30$; and (c) $K = 0.40$.

validate the assumed inception criteria and treatments for flows of this nature. The accuracy and effectiveness of the current cavitation model and algorithms are further demonstrated in these figures for a range of cavitation numbers by comparisons with experimental data. The strong influence of cavitation on pressure distribution and cavity shape is again highlighted in these figures. Regarding the influence of the cavitation number on the location of inception point, we can conclude from analysing the results for conic, hemispheric and ogival headform/cylinder bodies that, the influence becomes less when the curvature radium of the local surface of cavitation is smaller. It approaches to non-influence when the local surface becomes an edged corner, in which case the inception point is always fixed at the corner.

The current cavitation model and algorithm are well validated so far. The accuracy of the current model and treatments is found to be competent to those two-phase flow models proposed in the literature.

6. CONCLUSIONS

We reported a newly developed numerical treatment technique for attached cavitation and its application to some configurations. The cavitation model is implemented in a viscous Navier–Stokes solver. The cavity interface is assumed as a free surface boundary of the computation domain. Its shape is determined using an iterative procedure to match the cavity surface to a constant pressure boundary. The pressure distribution, as well as its gradient on the wall, is taken into account in updating the cavity shape iteratively. This method is validated by applying it to some typical configurations. The results obtained are reasonable and the iterative procedure of cavity shape updating is quite stable. The computations demonstrate the technique presented is valid. The lack of surface tension and a restriction to steady flow in the present cavitation model and algorithm is to be conducted in later research works.

NOMENCLATURE

C_p	pressure coefficient
C, λ	coefficient factors in formula
K	cavitation index
p	static pressure
p_V	vapour pressure
r	local thickness of a cavity
S^*	distance coordination along the wall surface
u, v, w, u_i	velocity components
$\vec{U}$	velocity vector
Z, R	cylindrical coordinates

Greek letters

α	local inclination angle of a cavity surface
μ	molecular viscosity
μ_{eff}	effective viscosity
μ_t	turbulent viscosity
ρ	fluid density

ACKNOWLEDGEMENTS

This work was partly supported by the Grants from Specialized Research Fund for the Doctoral Program of Higher Education (SRFDP) (20040698049) and Natural Science Foundations of Xi'an Jiaotong University in 2003. The authors would like to extend their appreciation to Prof. H. Tsukamoto of Kyushu Institute of Technology, Japan, and Dr T. Tanaka of Yatsushiro National College of Technology, Japan, for their helpful discussions.

REFERENCES

1. Brennen CE. *Cavitation and Bubble Dynamics*. Oxford University Press: Oxford, 1995.
2. Matsumoto Y. Bubble dynamics in cavitation. *Third International Symposium on Cavitation*. Grenoble: France, 1998; 3–8.
3. Jacqmin D. Calculation of two-phase Navier–Stokes flows using phase-field modeling. *Journal of Computational Physics* 1999; **155**:96–127.
4. Kunz RF, Boger DA, Stinebring DR, Chyczewski TS, Lindau JW, Gibeling HJ, Venkateswaran S, Govindan TR. A preconditioned Navier–Stokes method for two-phase flows with application to cavitation prediction. *Computers & Fluids* 2000; **29**:849–875.
5. Ahuja V, Hosangadi A, Arunajatesan S. Simulations of cavitating flows using hybrid unstructured meshes. *Journal of Fluids Engineering* 2001; **123**:331–340.
6. Schnerr GH, Sauer J. Physical and numerical modeling of unsteady cavitation dynamics. *Proceedings of the 4th International Conference on Multiphase Flow*, New Orleans, Louisiana, U.S.A., 2001.
7. Wang G, Senocak I, Shyy W, Ikohagi T, Cao S. Dynamics of attached turbulent cavitating flows. *Progress in Aerospace Science* 2001; **37**:551–581.
8. Senocak I. Computation methodology for the simulation of turbulent cavitating flows. *Ph.D. Dissertation*, University of Florida, Gainesville, U.S.A., 2002.
9. Rouse H, McNown JS. Cavitation and pressure distribution: head forms at zero angle of yaw. *Engineering Bulletin of State University of Iowa*, No. 32, 1948.
10. Singhal AK, Athavale MM, Li H, Jiang Y. Mathematical basis and validation of the full cavitation model. *Journal of Fluids Engineering* 2002; **124**:617–624.
11. Lindau JW, Kunz RF, Boger DA, Stinebring DR, Gibeling HJ. High Reynolds number, unsteady, multiphase CFD modeling of cavitating flows. *Journal of Fluids Engineering* 2002; **124**:607–616.
12. Wu J, Senocak I, Wang G, Wu Y, Shyy W. Three-dimensional simulation of turbulent cavitating flows in a hollow-jet valve. *Journal of Computational Modeling in Engineering and Science* 2003; **4**(6):679–689.
13. Wu J, Shyy W, Johansen ST. Filter-based unsteady RANS computations for single-phase and cavitating flows. HT-FED 2004-56181, *Proceedings of HT-FED'04*, *ASME Heat Transfer/Fluid Engineering Summer Conference*, Charlotte, North Carolina, U.S.A., 2004.
14. Deshpande M, Feng J, Merkle CL. Numerical modeling of the thermodynamic effects of cavitation. *Journal of Fluids Engineering* 1997; **119**:420–427.
15. Chen Y, Heister SD. Two-phase modeling of cavitated flows. *Computers and Fluids* 1995; **24**(7):799–809.
16. Visser FC. Some user experience demonstrating the use of computational fluid dynamics for cavitation analysis and head prediction of centrifugal pumps. FEDSM2001-18087, *Proceedings of ASME FEDSM'01*, *ASME Fluids Engineering Division Summer Meeting*, New Orleans, Louisiana, U.S.A., 2001.
17. Hirschi R, Dupont Ph, Avellan F, Favre JN, Guelich JF, Parkinson E. Centrifugal pump performance drop due to leading edge cavitation: numerical predictions compared with model tests. *Journal of Fluids Engineering* 1998; **120**:705–711.
18. Chen Y, Heister SD. A numerical treatment for attached cavitation. *Journal of Fluids Engineering* 1994; **116**:613–618.
19. Baldwin B, Lomax H. Approximate and algebraic model for separated flows. *AIAA Paper 78-257*, *AIAA 16th Aerospace Sciences Meeting*, Huntsville, AL, 1978.
20. Liu LJ. Computational and experimental investigations of steady and unsteady viscous flows in centrifugal compressor stages. *Ph.D. Dissertation*, Xi'an Jiaotong University, Xi'an, China, 1999.

